

Validation of Hermes-3 turbulence simulations against the TCV-X21 diverted L-mode reference case

B D Dudson¹, M Kryjak^{2,3}, H Muhammed^{2,3}, J Omotani³

¹ Lawrence Livermore National Laboratory, 7000 East Avenue, Livermore CA 94550, USA

² School of Physics, Engineering and Technology University of York, Heslington, York YO10 5DD, UK

³ United Kingdom Atomic Energy Authority, Culham Center for Fusion Energy, Culham Science Centre, Abingdon, OX14 3DB, UK

Abstract. Electrostatic flux-driven turbulence simulations with the Hermes-3 code are performed in TCV L-mode conditions in forward and reversed toroidal field configurations, and compared to the TCV-X21 reference dataset [D.S. Oliveira and T. Body *et al.* 2022] qualitatively and with a quantitative methodology. Using only the magnetic equilibrium, total power across the separatrix (120kW) and total particle flux to the targets ($3 \times 10^{21}/s$) as inputs, the simulations produce time-averaged plasma profiles in good agreement with experiment. Shifts in the target peak location when the toroidal field direction is reversed are reproduced in simulation, including the experimentally observed splitting of the outer strike point into two density peaks.

Differences between simulation and experiment include density profiles inside the separatrix and at the inner target in forward (favorable ∇B) field configuration. These differences in target temperature in forward field configuration lead to differences in the balance of current to the inner and outer divertor in the private flux region. The cause of these differences is most likely the lack of neutral gas in these simulations, indicating that even in low recycling regimes neutral gas plays an important role in determining edge plasma profiles. These conclusions are consistent with findings in [D.S. Oliveira and T. Body *et al.* 2022].

Keywords: TCV, validation, turbulence, tokamak

Submitted to: *Nucl. Fusion*

1. Introduction

The edge and divertor region of tokamak plasmas consists of the outermost part of the closed magnetic flux surfaces of the plasma core, and open magnetic field lines that intersect material surfaces. It is a transition region in which the flow of heat from the plasma core meets neutral gas and solid surfaces, and as such has a strong influence

on both plasma performance and plasma facing component lifetime. Understanding, predicting and controlling these flows of heat is a long-standing challenge [1] that requires a combination of multi-channel diagnostics, novel experiments, and sophisticated simulation models to address [2, 3].

Validation of plasma models is required to assess their reliability when applied to interpretation of current experiments or predictions for future devices. The TCV-X21 reference dataset [4], consisting of experimental data from the Tokamak à Configuration Variable (TCV [5]), has been published [6] and compared against drift-fluid simulations with GBS [7, 8], GRILLIX [9, 10], TOKAM3X [11, 12] and SOLEDGE3X [13], and the gyrokinetic code GENE-X [14]. The results of these studies are guiding rapid improvements in models of the boundary of magnetically confined fusion plasmas.

In this study we use the TCV-X21 dataset to validate the *Hermes-3* code [15, 16] that is built on BOUT++ [17]. Earlier versions of this code were compared to ISTTOK [18] Scrape-Off Layer (SOL) turbulence data but significant changes to the physical model and implementation have been made since then, including the addition of an ion pressure equation. The following section 2 describes the physical model and boundary conditions; results in forward and reversed magnetic field configuration are presented in section 3. We find differences in target conditions in forward magnetic field configuration, and focus on analysis of the currents flowing in the open field lines and through the sheath in section 4. Divertor heat fluxes, and flows of energy in the simulation are studied in section 5; Quantitative validation metrics are summarised in section 6; Conclusions are summarised in section 7.

2. Flux-driven turbulence model

Hermes-3 [15, 16] is capable of solving for multiple ion and neutral species, in 1-, 2- or 3-D domains to study steady-state, transient or turbulent phenomena. It is run here as a 6-field flux-driven turbulence model with a single ion species. Drift-reduced plasma fluid equations are solved for the electron density (n_e), electron and ion pressures (p_e, p_i) and electron and ion parallel momentum ($m_e n_e v_{||e}, m_i n_i v_{||i}$), and vorticity ω . These equations are derived from [19, 20, 21], modified as described in Appendix A. Drift-reduced fluid equations [22] are widely used in tokamak edge modeling and have a wide variety of complexity and implementations. Recently further improvements have been made in the formulation of these models [23], that are not incorporated into the equations used here.

The electron fluid equations for density n_e , parallel momentum $m_e n_e v_{||e}$, and pressure $p_e = e n_e T_e$ (where electron temperature T_e is in eV so that $e T_e$ has units of Joules, and all other quantities are in SI units) are:

$$\begin{aligned} \frac{\partial n_e}{\partial t} &= -\nabla \cdot [n_e (\mathbf{v}_E + \mathbf{b} v_{||e} + \mathbf{v}_{mag,e})] + S_n & (1) \\ \frac{\partial}{\partial t} (m_e n_e v_{||e}) &= -\nabla \cdot [m_e n_e v_{||e} (\mathbf{v}_E + \mathbf{b} v_{||e} + \mathbf{v}_{mag,e})] - \mathbf{b} \cdot \nabla p_e \end{aligned}$$

$$-en_e E_{||} + F_{ei} \quad (2)$$

$$\begin{aligned} \frac{\partial}{\partial t} \left(\frac{3}{2} p_e \right) = & -\nabla \cdot \left[\frac{3}{2} p_e (\mathbf{v}_E + \mathbf{b} v_{||e}) + \frac{5}{2} p_e \mathbf{v}_{mag,e} \right] - p_e \nabla \cdot (\mathbf{v}_E + \mathbf{b} v_{||e}) \\ & + \nabla \cdot (\kappa_{||e} \mathbf{b} \mathbf{b} \cdot \nabla T_e) + S_{Ee} + W_{ei} \end{aligned} \quad (3)$$

Where the electrostatic approximation is made, so that $E_{||} = -\mathbf{b} \cdot \nabla \phi$. Cross-field drift velocities are the $E \times B$ drift $\mathbf{v}_E = \frac{\mathbf{b} \times \nabla \phi}{B}$ and electron magnetic drift $\mathbf{v}_{mag,e} = -T_e \nabla \times \frac{\mathbf{b}}{B}$. The magnetic drift formulation is analytically equivalent to the diamagnetic drift form used in [21], but is easier to implement numerically in terms of conservative fluxes between cells [11]. S_n is the external source of particles; F_{ei} is the collisional (Braginskii [24]) friction between ions and electrons; S_{Ee} is an external source of power to the electrons, and W_{ei} is the collisional (Braginskii) exchange of heat between ions and electrons. Details of the collisional terms implemented are given in [15].

The ion fluid equations assume quasineutrality so that $n_i = n_e$, and evolve the ion parallel momentum $m_i n_i v_{||i}$ and pressure p_i :

$$\begin{aligned} \frac{\partial}{\partial t} (m_i n_i v_{||i}) = & -\nabla \cdot [m_i n_i v_{||i} (\mathbf{v}_E + \mathbf{b} v_{||i} + \mathbf{v}_{mag,i})] - \mathbf{b} \cdot \nabla p_i \\ & + Z_i en_i E_{||} - F_{ei} \end{aligned} \quad (4)$$

$$\begin{aligned} \frac{\partial}{\partial t} \left(\frac{3}{2} p_i \right) = & -\nabla \cdot \left[\frac{3}{2} p_i (\mathbf{v}_E + \mathbf{b} v_{||i}) + \frac{5}{2} p_i \mathbf{v}_{mag,i} \right] - p_i \nabla \cdot (\mathbf{v}_E + \mathbf{b} v_{||i}) \\ & + \nabla \cdot (\kappa_{||i} \mathbf{b} \mathbf{b} \cdot \nabla T_i) + S_{Ei} + S_n \frac{1}{2} m_i n_i v_{||i}^2 - W_{ei} \\ & + \frac{p_i}{en_0} \nabla \cdot (\mathbf{J}_{||} + \mathbf{J}_d) \end{aligned} \quad (5)$$

Where the ion magnetic drift is $\mathbf{v}_{mag,i} = T_i \nabla \times \frac{\mathbf{b}}{B}$. The final term in the ion pressure equation (5) is not in the original equations [21] but is required for energy conservation. See Appendix A.2 for details.

The vorticity ω can be derived from the divergence of the ion polarisation current, and is implemented in *Hermes-3* as:

$$\omega = \nabla \cdot \left[\frac{m_i n_0}{B^2} \nabla_{\perp} \left(\phi + \frac{p_i}{n_0} \right) \right] \quad (6)$$

where $\nabla_{\perp} \equiv \nabla - \mathbf{b} \mathbf{b} \cdot \nabla$ and the Oberbeck-Boussinesq approximation [25] is made, replacing the density in the polarisation current with a constant n_0 . The evolution of the vorticity is derived from current continuity, such that the divergence of the sum of all currents is zero: Polarisation current, parallel current $J_{||}$ and diamagnetic current J_d :

$$\begin{aligned} \frac{\partial \omega}{\partial t} = & -\nabla \cdot \left[\frac{m_i}{2B^2} \nabla_{\perp} (\mathbf{v}_E \cdot \nabla p_i) + \frac{\omega}{2} \mathbf{v}_E + \frac{m_i n_0}{2B^2} \nabla_{\perp}^2 \phi \left(\mathbf{v}_E + \frac{\mathbf{b}}{n_0 B} \times \nabla p_i \right) \right] \\ & + \nabla \cdot (\mathbf{J}_{||} + \mathbf{J}_d) \end{aligned} \quad (7)$$

Where the divergence of the diamagnetic current is:

$$\nabla \cdot \mathbf{J}_d = \nabla \cdot \left[(p_e + p_i) \nabla \times \frac{\mathbf{b}}{B} \right] \quad (8)$$

The vorticity equation (7) has been modified to improve energy conservation in the model, as described in Appendix A.1.

The ion viscosity derived in [19, 20, 21] is not included in these simulations, and does not include the neoclassical correction recently implemented in GRILLIX [26], that replaces τ_i with a combination of τ_i and ion bounce time. We plan to implement similar improvements in future work that targets lower collisionality regimes than are simulated here.

2.1. *Boundary conditions*

In the radial direction Neumann (zero gradient) boundary conditions are applied to plasma density and pressures on both inner (core) and outer (scrape-off layer) boundaries. A Dirichlet (zero value) boundary is applied to the parallel flow of both electrons and ions at both radial boundaries.

The calculation of the electrostatic potential ϕ from vorticity ω is by inverting an elliptic equation (6) at every time step iteration. The linear solve is performed in toroidal planes, invoking the flute approximation to drop poloidal derivatives that couple toroidal planes, as is usually done in BOUT++ models [17]. We wish to impose zero-gradient boundary conditions on ϕ at both boundaries, to allow poloidal variation of the potential around the SOL and to avoid constraining the potential at the core boundary. This would lead to an ill-posed linear solve due to the null space of the operator. Instead, we use a method adapted from STORM [27, 28]: Dirichlet boundary conditions are used in the linear solve for ϕ , so that the inversion is well posed, but the value of the boundaries relaxes towards zero-gradient on a short timescale, here chosen to be $1\mu s$.

At the sheath (target) boundaries Bohm-Chodura-Riemann boundary conditions are applied [29], using the multi-ion magnetized sheath condition derived in [30]. This imposes sonic ion flow into the sheath, with a sheath heat transmission that depends on the potential ϕ . The potential at the sheath entrance is not fixed; instead currents flow into or out of the sheath until a (quasi-) steady-state potential is reached. This can lead to quite complex patterns of plasma currents closing through the sheath that are analysed in section 4.

2.2. *Sources and geometry*

Hermes-3 simulations are flux-driven with prescribed spatially-varying sources of particles, electron and ion heating. There are no neutrals in the simulations shown here, so the experimentally inferred target particle flux of 3×10^{21} particles per second [4] is injected into the simulation domain in a thin region near the core boundary. 120kW of heating power is injected, divided equally between electrons and ions, and distributed evenly in poloidal angle near the core boundary using the same source profile as the particle source. Heat and particles flow to the divertor targets, where they are removed through the sheath boundary conditions at the target plates. In these simulations there

are no neutrals and so no particle recycling: All particles arriving at the sheath are removed from the simulation.

Simulations are performed in tokamak geometry using the curvilinear shifted metric coordinate system usually used in BOUT++ [17]. The tangential basis vectors are a radial coordinate (x) in the direction of $\nabla\psi$, a poloidal coordinate (y) that is aligned to the magnetic field direction, and a toroidal angle coordinate (z). Aligning the poloidal coordinate with the magnetic field enables a coarse poloidal resolution to be used while resolving small-scale field-aligned turbulent structures, but at the cost of introducing a coordinate singularity at the X-point, so that the region around the X-point is poorly resolved in the poloidal plane. Meshes are constructed using the Hypnotoad tool [31].

Two TCV equilibria are studied here: A “forward” (+) toroidal magnetic field configuration favorable ∇B , with ion magnetic drift $\mathbf{v}_{mag,i}$ downwards towards the X-point; and a “reverse” (−) toroidal field configuration in which the ion magnetic drift is upwards.

2.3. Numerical methods

Conservative finite difference methods are used in *Hermes-3*, with cross-field drifts as described in [32] and parallel dynamics in [15, 33]: All quantities are cell centered, and 2nd-order operators are formulated in terms of fluxes between cells; The Monotonised Central (MC) limiter is used to reconstruct cell edge values from cell center values. In the direction along the magnetic field a Lax flux is used to stabilise grid-scale oscillations, taking the electron thermal speed as the fastest wave in the system. Time integration is fully implicit with an adaptive order and timestep, implemented in the SUNDIALS CVODE library [34].

Simulations shown here were performed using parameters shown in table 1.

Table 1: Simulation mesh parameters

Mesh size (ψ, θ, ζ)	$64 \times 32 \times 81$
Fraction of a torus	1/5
Radial resolution [mm]	0.3 - 7.6
Binormal resolution [mm]	0.2 - 3.0
Sound gyro-radius [mm]	0.1 - 1.4

The resolution of the mesh should be sufficient to resolve the plasma “blob” structures, typically on the scale of a few to tens of ion sound gyroradii $\rho_s = \sqrt{eT_e/m_i} (m_i/eB)$. This scale-length depends on the local plasma temperature, so must be calculated in post-analysis. Figure 1b shows the ratio of radial grid spacing dr to ρ_s , using time-averaged temperature profiles from the *Hermes-3* simulation. It can be seen that the turbulence scales are well resolved (light yellow) close to the separatrix, in both closed field-line region and divertor legs. In the outer scrape-off layer (SOL)

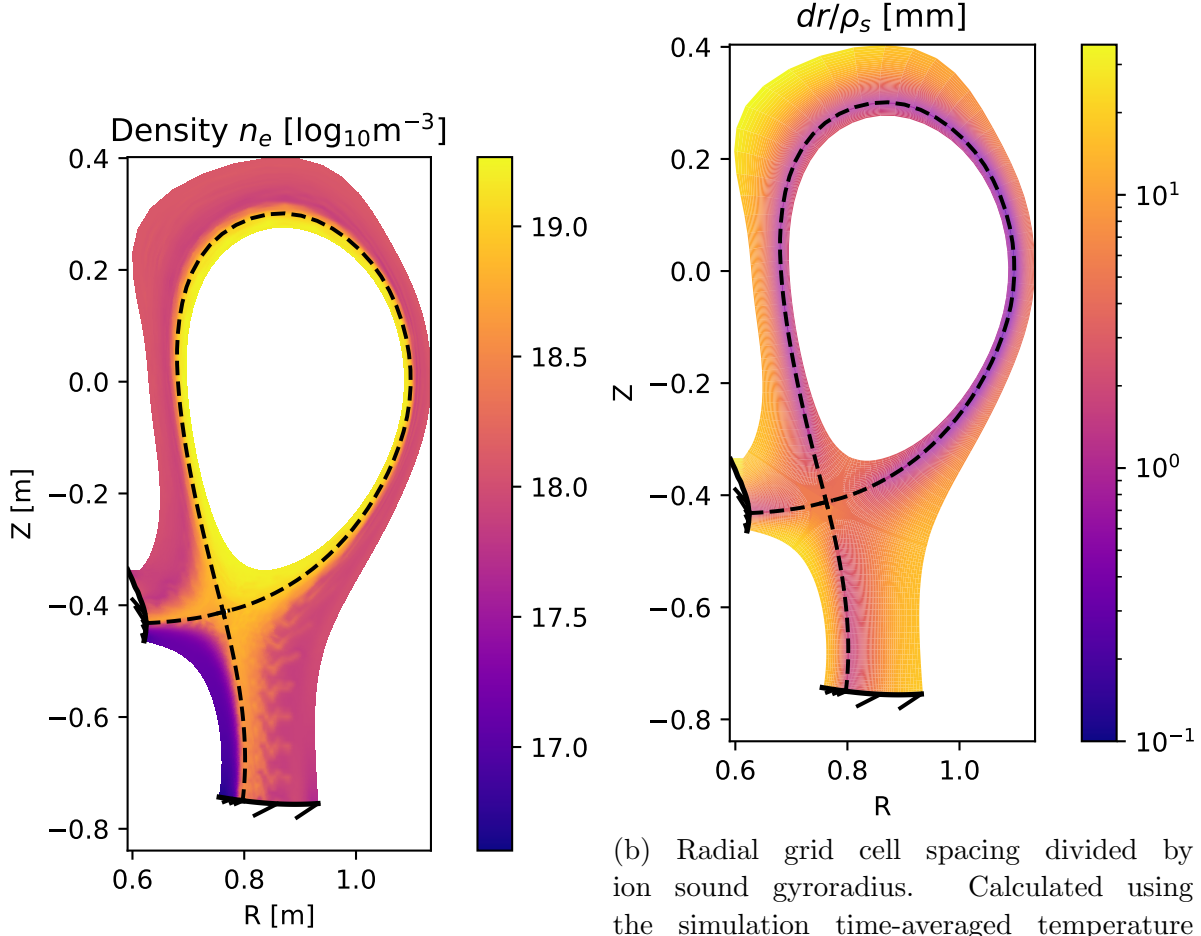


Figure 1: Poloidal slices through the 3D domain in the forward field configuration. The simulations solve for an annulus around the separatrix, and do not solve for the core region.

and private flux region (PFR) the electron temperature is low and the mesh is unable to resolve the smallest scales. We therefore expect best agreement between simulation and experiment in the near SOL in the following sections.

3. Results

In the following results the forward field simulation was run for 7.3ms, with results taken from the last 1.9ms. The reversed field simulation was run for 6.9ms, with results taken from the last 1.9ms. The computational cost at this low resolution was approximately 6×10^3 core-hours per ms of simulation time, running on 64 cores.

3.1. Midplane profiles

A summary of separatrix quantities from experimental measurements [4] and *Hermes-3* simulations is given in table 2. The temperature and temperature scale-length in the

Table 2: Separatrix parameters at outboard midplane in forward toroidal field configuration

	Hermes-3	TCV
Separatrix T_e [eV]	39 ± 3	35 ± 5
T_e width, λ_T [cm]	0.8 ± 0.1	1.0 ± 0.4
Separatrix n_e [10^{18}m^{-3}]	11.7 ± 1.5	6.7 ± 0.8
n_e width, λ_n [cm]	0.5 ± 0.1	0.9 ± 0.2

near Scrape-Off Layer (SOL) are quite well matched (within one standard deviation). The *Hermes-3* simulations however have separatrix densities that are higher than experiment, by a factor of ~ 1.8 . We hypothesize that this difference in density is due to the different particle source locations, since the total particle flux to the targets is approximately matched: In experiment neutrals are ionized in the divertor leg, whereas in these simulations the only source of particles is in the closed field-line region.

Radial profiles of density n_e , electron temperature T_e and plasma potential ϕ are shown in figure 2. Solid lines show experimental data, and dashed lines the *Hermes-3* simulation. As previously, shaded regions indicate the standard deviation of the data. Forward (favorable ∇B) configuration is plotted in blue, and reverse configuration in red.

In both forward and reverse configuration the density profiles (figure 2a) are higher in simulation than experiment, as shown in table 2. In both experiment and simulation we see that the density is higher in forward-field configuration (blue lines) than reversed (red).

The electron temperature is quite insensitive to the magnetic field direction, both at the midplane (figure 2b) and at the targets (figures 3b and 4b). The simulation and experimental profiles are within error bars (shaded region), but the simulation is systematically cooler than experiment in the far SOL and has lower fluctuation levels, shown as narrower shaded regions.

In both experiment and simulation the plasma potential (figure 2c) shifts with the change in toroidal magnetic field, so that the potential in the SOL is higher with reversed toroidal field than forward field. The temperature profiles are largely unchanged, so this shift is likely to be dominated by the diamagnetic drift direction rather than changes in the sheath potential with electron temperature. At the low-field side target (figure 3c) the same shift in potential is seen, accompanied by changes in time-averaged current into the sheath (figure 3d), that will be discussed in section 4.

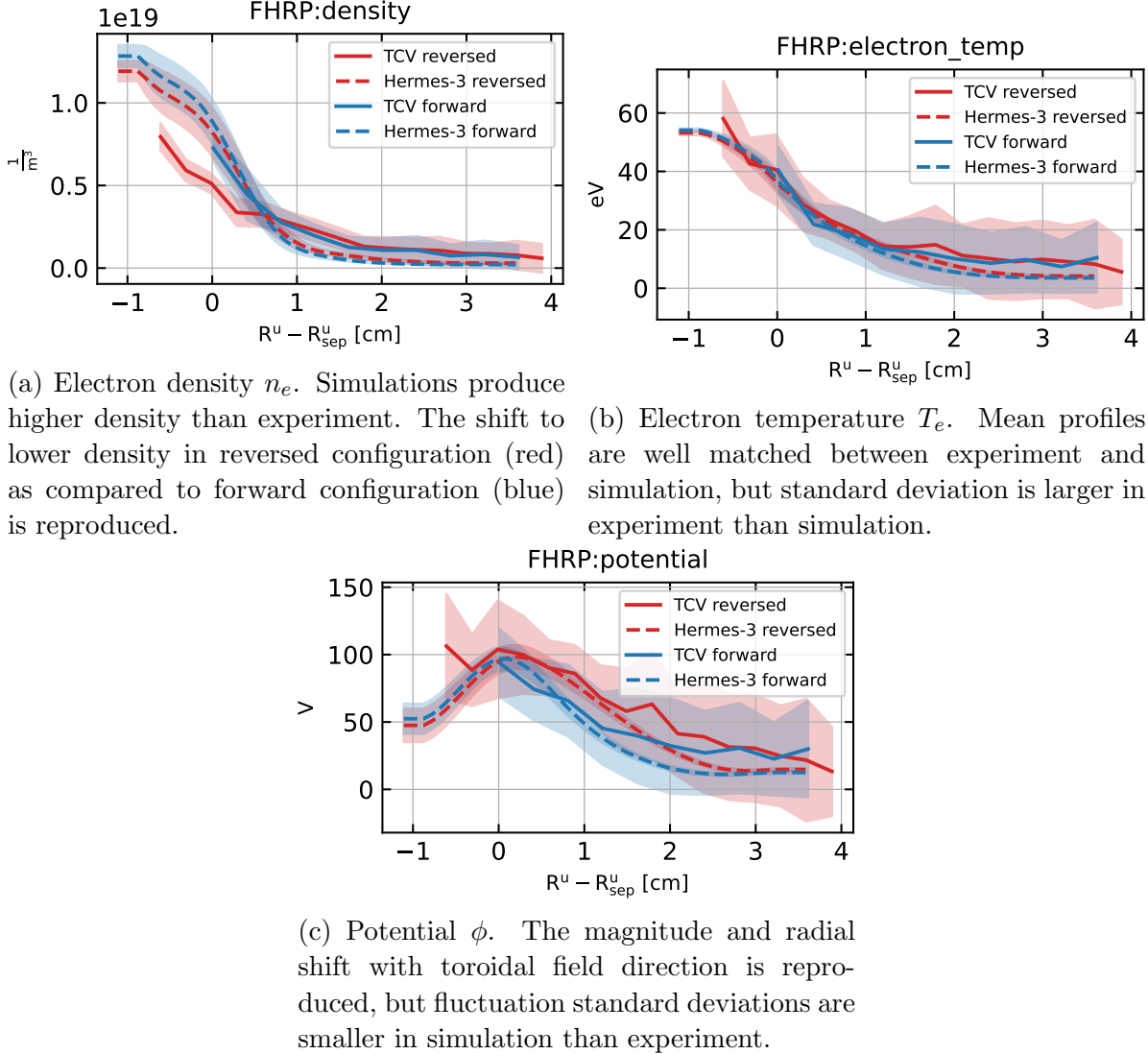


Figure 2: Midplane profiles. Forward field cases are shown as blue lines, and reversed field as red lines. Experimental data are solid lines, and Hermes-3 simulations are dashed.

3.2. Low-field side divertor target

Density, temperature, potential and current profiles measured using Langmuir probes at the low-field (outboard) divertor target are shown in figure 3. The radial coordinate $R_u - R_{sep}$ is the distance from the separatrix at the outboard midplane, mapped in poloidal flux ψ from the divertor target. Locations in the PFR are not connected to the outboard midplane, so the mapping is to the flux surface in the core with the same ψ value as the PFR flux surface. There is a qualitative change in the density profile (fig 3a) between forward and reversed field cases: In the reversed field case a single peak is seen in both experiment and simulations, at a midplane-mapped location of $R^u - R_{sep}^u \simeq 0.3$ cm. When the toroidal field is in the forward direction, Hermes-

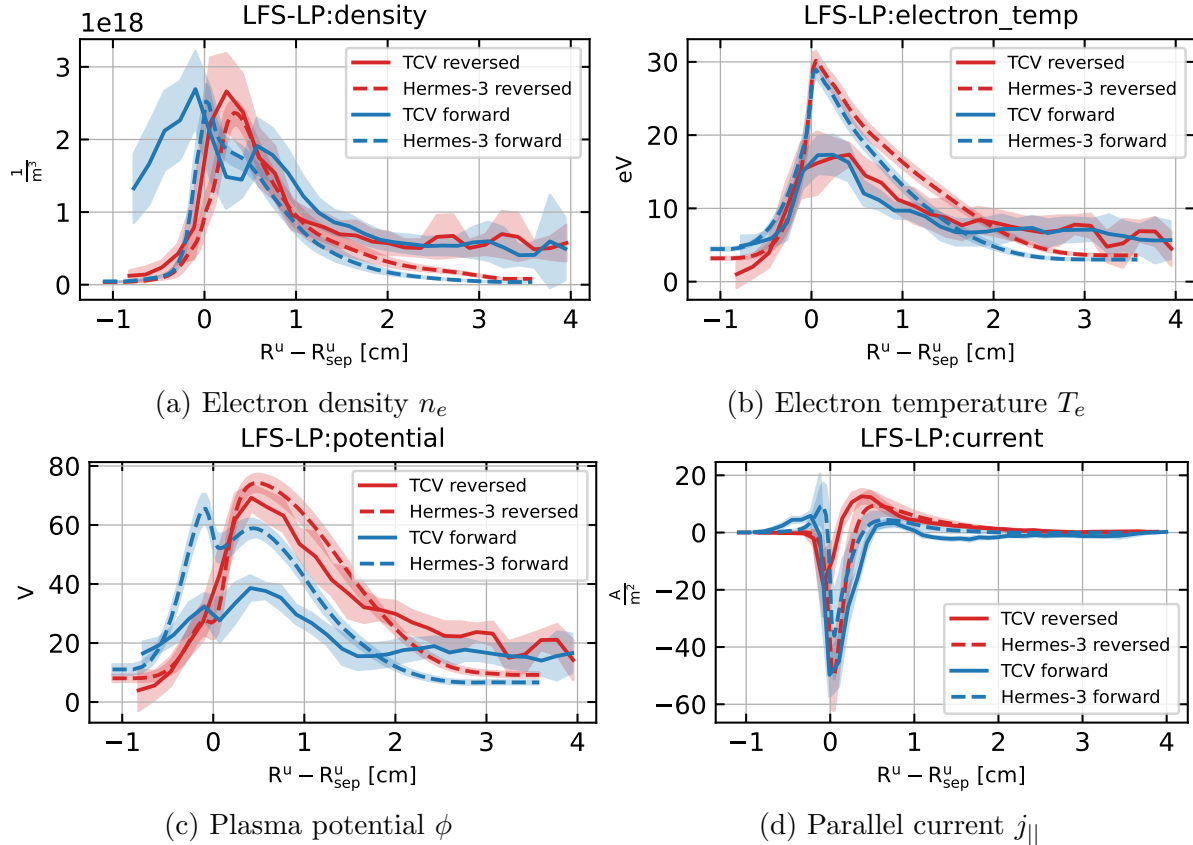
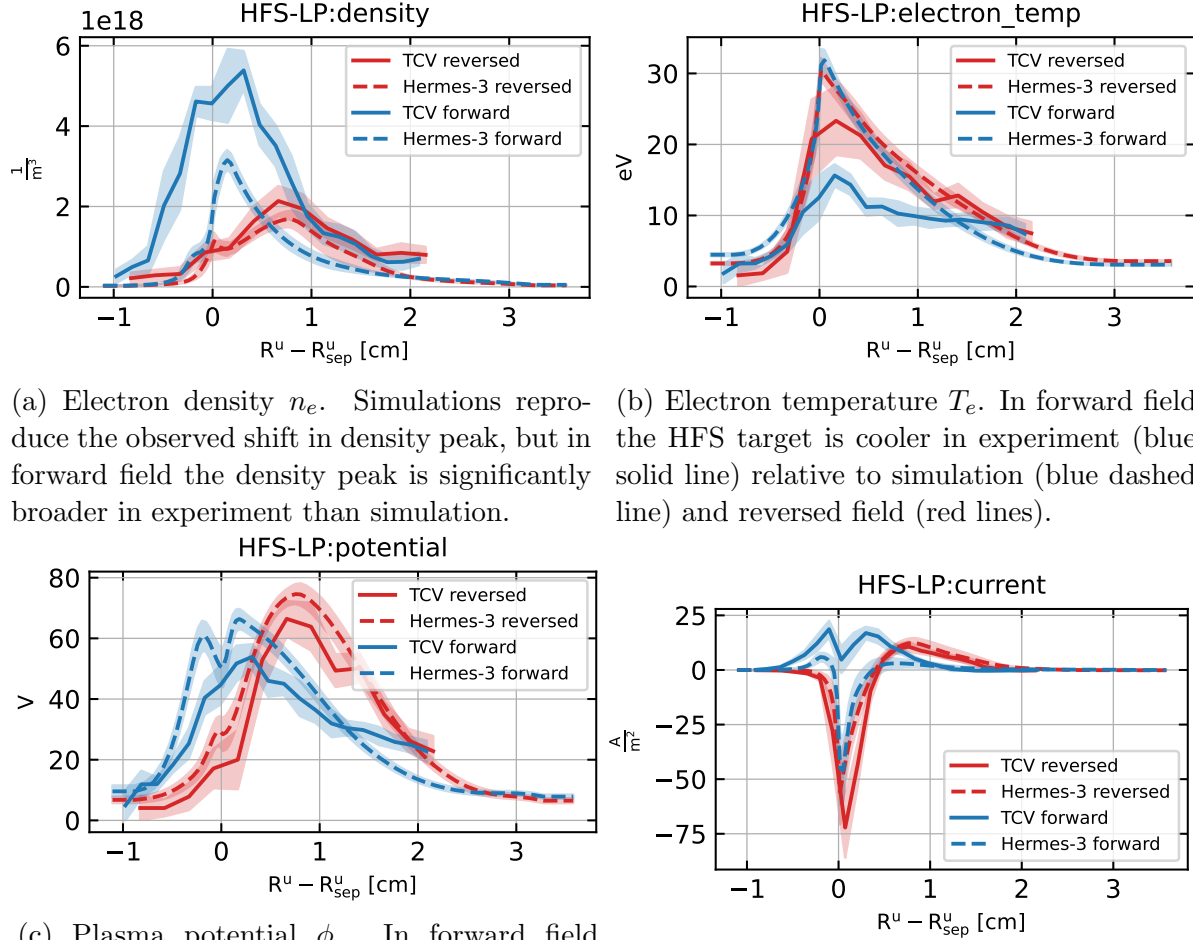


Figure 3: Low-Field Side (LFS) divertor profiles. Forward field cases are shown as blue lines, and reversed field as red lines. Experimental data from Langmuir probes are solid lines, and *Hermes-3* simulations are dashed. All profiles are mapped along flux surfaces in ψ space from divertor target to major radius R^u at midplane.

3 reproduces the experimentally observed broadening of the density peak, sometimes splitting into two peaks like the potential ϕ , with the location of maximum density shifting towards the separatrix. There is however a notable difference in the density between simulation and experiment in the PFR of the forward-field case. This could be caused by stronger transport into the PFR from the SOL in experiment, or due to ionization sources that are present in experiment but not simulation.

As with the midplane profiles, the temperature profiles (figure 3b) are quite insensitive to field direction, particularly near the separatrix. Simulation temperatures are more peaked, and systematically higher, than experiment. Going from forward (blue) to reversed (red) there is reduction in the PFR temperature and increase in the SOL temperature, in both experiment (solid) and simulation (dashed).

The plasma potential (figure 3c) is well matched in reverse field configuration (red lines), though *Hermes-3* does not reproduce the relatively flat profiles of electron temperature and potential in the far SOL. This may be related to the far SOL being under-resolved (figure 1b). In the forward field configuration (blue lines) both experiment and simulation show two peaks in potential, though the PFR has a much



(a) Electron density n_e . Simulations reproduce the observed shift in density peak, but in forward field the density peak is significantly broader in experiment than simulation.

(b) Electron temperature T_e . In forward field the HFS target is cooler in experiment (blue solid line) relative to simulation (blue dashed line) and reversed field (red lines).

(c) Plasma potential ϕ . In forward field the potential is higher in simulation than experiment in the Private Flux region (PFR), $R^u - R^u_{sep} < 0$.

(d) Parallel current $j_{||}$. In forward field the current in experiment has the opposite sign to experiment.

Figure 4: High-Field Side (HFS) divertor profiles. Forward field cases are shown as blue lines, and reversed field as red lines. Experimental data from Langmuir probes are shown as solid lines, and Hermes-3 simulations are dashed lines. All profiles are mapped along flux surfaces in ψ space from divertor target to major radius R^u at midplane. Hermes-3 agrees well with experimental profiles in reversed field, but not in forward field.

higher voltage in simulation than experiment. In this forward configuration the PFR sheath is in the ion saturation regime, so that large changes in potential ϕ cause only small changes in sheath current $j_{||}$ (figure 3d). In section 4 the currents into the sheath are analysed in more detail.

3.3. High-field side divertor target

Plasma profiles at the inboard (high-field side, HFS) target are shown in figure 4. Hermes-3 simulations are able to match well the density, electron temperature, potential and parallel current profiles at the high-field side target in the reversed field configuration

(red lines in figure 4). Simulations reproduce features of the target profiles including density peaking in the SOL ($R^u - R_{sep}^u \simeq 0.8\text{cm}$), the location of the sign reversal in the parallel current ($R^u - R_{sep}^u \simeq 0.5\text{cm}$), and both shape and magnitude of the plasma potential profile.

Going from reversed field (red) to forward field (blue) case, the density peak (figure 4a) shifts closer to the separatrix in both simulation and experiment, but in experiment the peak is significantly broader than in simulation. The temperature (figure 4b) also shifts, but is significantly lower in experiment in the forward magnetic field than reverse field.

A striking difference between simulation and experiment is the parallel current into the sheath (figure 4d) that is quite well matched between simulation and experiment in reversed field, but different in forward field. The reversed field case shows that if the density, temperature and potential (figure 4c) are comparable between experiment and simulation, then the parallel current also agrees. This indicates that the sheath boundary condition implemented in *Hermes-3* [30] is consistent with the sheath characteristics assumed in the Langmuir probe analysis in this plasma regime. In the next section we examine in more detail the currents in forward and reversed magnetic field configurations, in order to understand the observed differences.

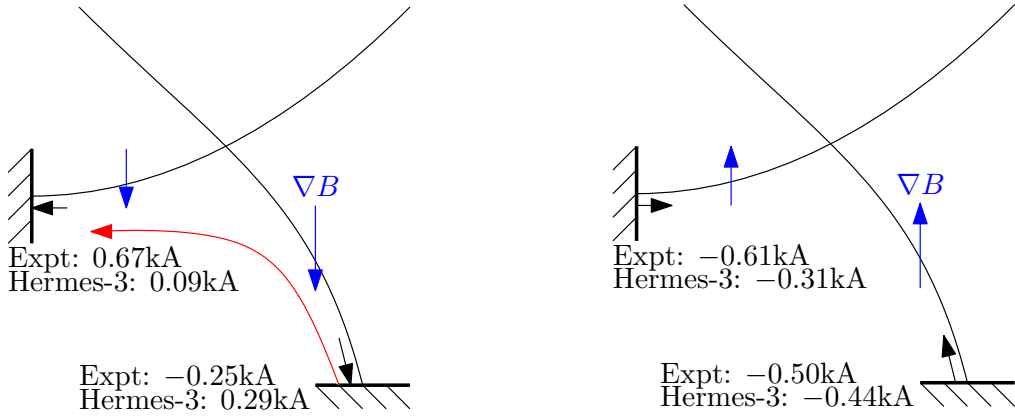
4. Sheath currents

The currents in the SOL and PFR are determined by combination of diamagnetic, polarisation and parallel currents, complicated by the nonlinear and asymmetric response of the sheath to electrostatic potential perturbations: In these simulations the wall is conducting so that the current through the sheath into the wall [30] has the form of equation 9.

$$j_{sh} \simeq nc_s [1 - \exp(-\phi/T_e)] \quad (9)$$

and goes to zero when the potential $\phi \simeq 2.8T_e$ for a deuterium plasma. In general the current is non-zero, depending nonlinearly on the local temperature, density and potential. The balance of currents changes when the magnetic field is reversed, because the magnetic drift (equivalently, diamagnetic current) reverses direction.

In the forward field case we find good agreement in the parallel current at the low field side (blue lines in figure 3d), but not at the high-field side (blue lines in figure 4d) where the *Hermes-3* current is more negative (out of the target) than experiment. In reversed field configurations we find good agreement at the high-field side (red lines in figure 4d), with good agreement in the density, electron temperature, and plasma potential, particularly in the region $R^u - R_{sep}^u \simeq 0 - 0.5\text{cm}$. At the low-field side, however, (red lines in figure 3d) the simulation time-averaged current is more negative than measured experimentally.



(a) Forward field. Downward ∇B currents (blue arrows) are balanced by Plate Closing Currents (PCC) into the sheath (black arrows). In experiment an additional thermoelectric current (red arrow) flows from outer to inner target, reversing the current at the outer (LFS) target.

(b) Reverse field. Upward ∇B currents (blue arrows) are balanced by Plate Closing Currents (PCC [35]) out of the sheath (black arrows).

Figure 5: Currents into and out of the Private Flux Region (PFR), in (a) forward (favorable ∇B) and (b) reverse (unfavorable ∇B) toroidal field configurations.

4.1. Currents in the Private Flux Region

The analysis of currents into the sheaths is simplified by considering the PFR, because the magnetic topology isolates it from the core plasma dynamics. The currents into and out of the PFR are sketched in figure 5 for both forward and reversed field. In reverse (unfavorable) configuration, ion ∇B and curvature drifts drive a current from the PFR upwards into the SOL. This is balanced by Plate Closing Currents (PCC) from the plasma into the sheath [35], illustrated in figure 5b. The total current into both targets is similar between experiment (-1.1kA) and *Hermes-3* simulation (-0.75kA), and is divided approximately equally between inner (HFS) and outer (LFS) targets: At HFS target the experimentally measured current in the PFR is -0.61kA , simulated is -0.31kA ; at LFS the experimentally measured current is -0.50kA , and simulated is -0.44kA .

In forward (favorable) configuration, ion ∇B and curvature drifts drive a current from the SOL into the PFR, so that net current into the PFR reverses sign relative to the reverse configuration. As in reversed field configuration, the magnitude and direction of the total current to the targets is similar: experiment 0.42kA , simulation 0.38kA . In this case the currents at the two targets are quite different between experiment and simulation. At the high-field side (HFS) target the experiment measured 0.67kA into the PFR, but simulation only 0.09kA ; At the low-field side (LFS) the experimentally measured -0.25kA is opposite in sign to the 0.29kA predicted in simulation.

We attribute this difference to a strong thermoelectric current from outer (LFS) to

inner (HFS) targets in the PFR [36] that is present the experiment but not simulation, due to differences in target temperatures. As discussed in section 3.3, the temperature at the inner (HFS) target in forward field configuration (figure 4b) is significantly cooler in experiment than simulation, perhaps due to cooling by neutral recycling that is present in experiment but not simulation. The current into the sheath is approximately given by equation 9. At the LFS the potential is less than $2.8T_e$ ($T_e \sim 15\text{eV}$, $\phi \sim 30\text{V}$), whereas at HFS the potential is above this threshold ($T_e \sim 12\text{eV}$, $\phi \sim 40\text{V}$). The lower temperature at HFS therefore drives a positive current into the HFS target, drawn from the higher temperature LFS target.

In summary, in both forward and reverse field cases the total current to both targets is similar between experiment and simulation, being determined by the magnetic drift current across the separatrix. The balance of currents between the target plates shows differences that correlate to cooling of the inner target. This is likely to be due to plasma-neutral interactions that are not included in these simulations.

5. Divertor heat fluxes and power balance

The heat flux through the sheath and into the divertor targets due to electrons and ions is the heat flux $q_{||}$ along the magnetic field:

$$q_{||e,i} = \gamma_{e,i} e n_{e,i} T_{e,i} C_i \quad . \quad (10)$$

The electron and ion sheath heat transmission factors, γ_e and γ_i , are calculated for a single ion species as [30]:

$$\gamma_e = 2 + (\phi_{sheath} - \phi_{wall}) / T_{e,sheath} \quad (11)$$

$$\gamma_i = 2.5 + \frac{1}{2} M_i C_i^2 / e T_{i,sheath} \quad (12)$$

Where the ion sheath velocity $C_i^2 = e (5/3 T_i + T_e) / M_i$. In these simulations γ_e varies between 3.5 and 9 over time and space, with time-averaged values varying in space between 4 and 7.5. The time-averaged ion heat transmission factor, γ_i varies between 3.5 and 4.5.

Experimentally the heat flux is measured using an infrared (IR) camera [4], with target surface heat flux mapped to parallel heat flux. Results are shown in figure 6 for forward and reverse field configurations. Note that the simulation heat fluxes do not include surface recombination energy that is present in experiment. *Hermes-3* simulations produce a higher peak power density at the LFS divertor but a lower total power to the outboard target than experiment. Possible explanations for the additional broadening in experiment include differences in plasma turbulence, radiated power, and other neutral interactions.

Integrating heat fluxes across the outboard (LFS) divertor in figure 6 provides total powers shown in table 3. Only LFS target heat flux is measured by the IR camera, but the simulation heat fluxes at both targets are given. *Hermes-3* simulations find that in forward (+) configuration the power balance is approximately equal between LFS and

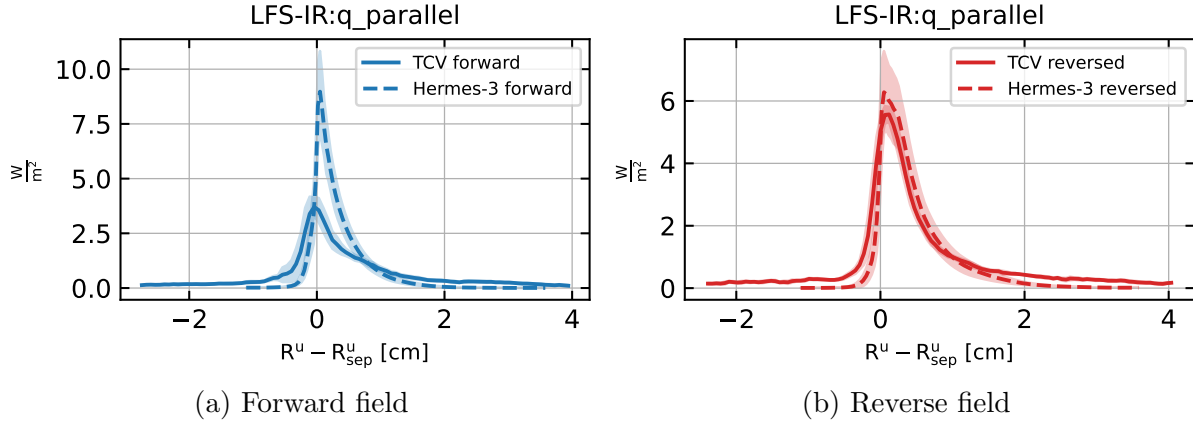


Figure 6: Solid lines: Parallel heat flux at the outboard (LFS) target as measured by infrared (IR) camera diagnostic, mapped in poloidal flux space to the outboard midplane. Dashed lines: Hermes-3 simulation. Shaded areas in the simulation data indicate a standard deviation of the heat flux, over time and toroidal angle.

Table 3: Power in kW to outboard (LFS) and inboard (HFS) divertor targets in forward (+) and reverse (-) configurations. TCV experimental results at LFS are obtained by integrating infrared (IR) camera measurements (figure 6). Simulation results do not include surface recombination power.

		Hermes-3 (+)	TCV (+)	Hermes-3 (-)	TCV (-)
LFS	Total	39	36.5	40	46.5
	Electron	21		21	
	Ion	18		19	
HFS	Total	37		30	
	Electron	20		14	
	Ion	17		16	

HFS divertor targets, while in reverse (-) configuration more power goes to the LFS target than HFS.

As described in section 2.2, both forward and reverse simulations are driven by 120kW of heating power inside the separatrix, 60kW into each species. We should therefore expect a similar power to arrive at the divertor targets. To understand the discrepancy between input power and power arriving at the target plates in these simulations, we have instrumented Hermes-3 with diagnostics to track energy flows and transfer channels that are described in Appendix B. Taking the forward field case, integrating energy transfer channels over the domain and averaging over time, we obtain results shown in figure 7.

The energy flows in figure 7 are averaged over the domain and a period of $78\mu\text{s}$. The system has reached quasi-steady state, such that the rate of change of the thermal

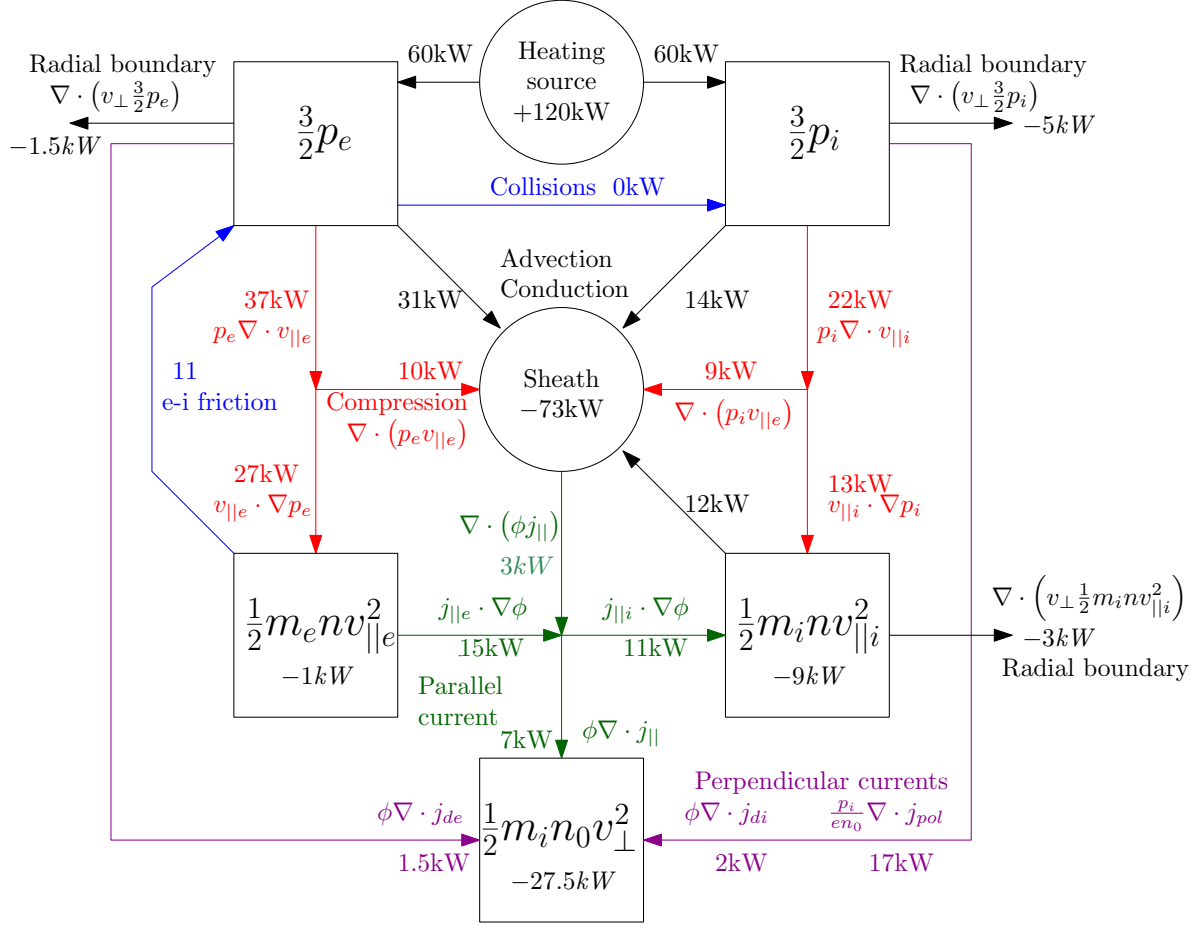


Figure 7: Forward field energy flow analysis. Energy flows from the heating source into thermal energy ($\frac{3}{2}p_{e,i}$) and from there to perpendicular kinetic energy ($\frac{1}{2}m_i n_0 v_{\perp}^2$), parallel electron and ion kinetic energy ($\frac{1}{2}m_{e,i} n_0 v_{||e,i}^2$), before being deposited in the sheath, transported to radial boundaries, or lost in numerical dissipation. Positive numbers indicate heat sources and transfer channels; negative numbers indicate energy sinks. The heating source and sheath sink are shown as circles; Energy forms as square boxes, with negative numbers indicating the energy imbalance (if any). Energy transfer channels are labeled with approximate energy flow in kW, and are colored to indicate parallel advection and conduction (black); parallel compression (red); parallel currents (green); perpendicular currents (magenta); and collisions (blue). See Appendix B for details.

energy in the system is less than 0.1kW over this averaging period. Nevertheless, the energy fluxes given here have uncertainties and should be considered approximate: The Root-Mean-Square (RMS) value of the energy transfer channels are orders of magnitude larger than their averages. For example, the transfer $\frac{p_i}{en_0} \nabla \cdot j_{pol}$ between ion thermal and perpendicular kinetic energy has an RMS value of around 0.7MW/m³ and peak values (positive and negative) of order 20MW/m³. The volume of the domain is 1.3m³, so fluctuations are significant as compared to the mean power flows through the system.

We therefore do not expect exact balance between energy flows over time averaging periods shorter than the energy confinement time. The analysis here has been repeated for averages over short time windows of 0.1ms and 0.2ms, finding qualitatively the same results.

Electron and ion thermal energy are conserved well: Each have 60kW of heating power that balances losses to within 1kW. This conservation is expected because species pressures are evolved by exchanging fluxes between cells. Of the 120kW input power, approximately 6.5kW is transported as thermal energy to the radial domain boundaries (walls).

Electron and ion parallel kinetic energy ($\frac{1}{2}m_en_0v_{||e}^2$ and $\frac{1}{2}m_in_0v_{||i}^2$) are not evolving variables, but are derived from evolution of momentum and density. Electron parallel kinetic energy is driven by the parallel electron pressure gradient (27kW), dissipated by electron-ion friction (11kW) and parallel electric fields (15kW). Approximately 1kW is unaccounted for in the electron parallel kinetic energy balance, and is likely being lost as numerical dissipation. Similar analysis of the ion parallel kinetic energy finds approximately 9kW imbalance. In the transfer terms involving parallel currents $j_{||}$ and electric potential ϕ (colored green in figure 7) there is an energy flow $\int \phi j_{||} \cdot dS$ of order 3kW out of the sheath. This energy flow accounts for the difference between the total power to the divertor targets given in table 3 for forward field (76kW), and the total power to the sheath in figure 7 (73kW).

The ion perpendicular flow ($\frac{1}{2}m_in_0v_{\perp}^2$) is also a derived quantity, being related to the vorticity equation (see Appendix B). We observe a transfer of approximately 27.5kW to perpendicular ion motion, mainly from ion thermal energy (19kW) and the $\phi \cdot j_{||}$ channel (7kW). This power (27.5kW) is likely being lost either to radial boundaries (diagnostics for transport of perpendicular ion kinetic energy through the boundaries have not yet been implemented) or to dissipation, but not being returned to thermal energy in the present simulations. A significant amount of power (17kW) is seen to be transferred from ion thermal energy to perpendicular motion via the divergence of the polarisation current term $\frac{p_i}{en_0} \nabla \cdot j_{pol}$ that is discussed in Appendix A.2. The size of this term, and the power discrepancies we observe, highlight the importance of theoretical work to improve energetic consistency of drift-reduced models [23] and treatment of the polarisation drift.

In summary, analysis of energy transfer channels indicates that of the 120kW input power approximately 73kW goes to the divertor targets, 9.5kW goes to the radial boundaries, and the remaining 37.5kW is dissipated: 9kW from ion parallel kinetic energy, and 27.5kW from ion perpendicular energy. The system has reached quasi-steady state, but these numbers are approximate due to the large fluctuations.

These findings, and the energy flow analysis tools implemented here, will be used to direct future improvements in the *Hermes-3* model and numerical implementation.

6. Quantitative Validation

In this section the validation methods included with the TCV-X21 dataset [6] are applied to *Hermes-3* simulation output. After translation into a standardized format, the shared analysis toolchain ensures as far as possible a consistent comparison between experiment and the outputs of different simulation codes. The validation methodology is detailed in [4, 37], briefly summarised here.

Each row in the table below corresponds to an observable labelled j from a particular diagnostic e.g. electron density from the reciprocating Langmuir probe. This observable has N_j measurements labelled $i = 1 \dots N_j$ e.g. density at different radial locations. The experimental measurement i of an observable j is $e_{j,i}$ with uncertainty (standard deviation) $\Delta e_{j,i}$. Similarly, the simulation produces a value of $s_{j,i}$ with uncertainty $\Delta s_{j,i}$.

The normalised difference d_j between simulation and experiment for an observable j is defined in equation 13:

$$d_j = \left[\frac{1}{N_j} \sum_{i=1}^{N_j} \frac{(e_{j,i} - s_{j,i})^2}{\Delta e_{j,i}^2 + \Delta s_{j,i}^2} \right]^{1/2}. \quad (13)$$

The level of agreement $R(d_j)$ smoothly varies from 0 for perfect agreement ($d_j = 0$) to 1 for disagreement ($d_j \gg 1$).

$$R(d_j) = \frac{\tanh [(d_j - 1/d_j - 1) / 0.5] + 1}{2}. \quad (14)$$

The sensitivity S_j of an observable j is a measure of the precision of the comparison

$$S_j = \exp \left(- \frac{\sum_i \Delta e_{j,i} + \sum_i \Delta s_{j,i}}{\sum_i |e_{j,i}| + \sum_i |s_{j,i}|} \right). \quad (15)$$

S_j approaches 1 for high precision measurements, and 0 if uncertainties are large.

The level of agreement $R(d_j)$ and sensitivities S_j for a set of observables are combined into a composite metric χ that varies between 0 (agreement) and 1 (disagreement):

$$\chi = \frac{\sum_j R(d_j) H_j S_j}{\sum_j H_j S_j}. \quad (16)$$

Where H_j is a Hierarchy weighting that is 1 for observables that are directly measured and simulated, smaller than 1 for derived quantities. Table 1 of [4] lists H_j for all observables used here. The denominator of equation 16 is the ‘quality’

$$Q = \sum_j H_j S_j \quad (17)$$

that is higher for validations using more directly computed, higher precision observables. Table 4 below lists the normalised difference d_j and sensitivity S_j for each observable. These are grouped into diagnostics, with a composite metric χ and quality Q . Finally an overall metric and quality are computed by combining all diagnostics.

Table 4: Quantitative validation result for each observable, in forward (+) and reversed (-) toroidal field direction. For each observable the normalized difference between experiment and simulation d_j (equation 13) and sensitivity S_j (equation 15) are calculated. The color scale is limited to $0 < d_j < 5$; Green cells indicate good agreement ($d_j \lesssim 1$) and red cells indicate poor agreement ($d_j \gtrsim 4$). Observables are combined into a composite metric χ (equation 16) and validation quality Q (equation 17).

Diagnostic	observable	Hermes(+)		Hermes(-)	
		d_j	S	d_j	S
Fast horizontally-reciprocating probe (FHRP) for outboard midplane	n	1.01	0.76	1.44	0.817
	T_e	0.388	0.69	0.331	0.745
	V_{pl}	0.409	0.688	0.467	0.73
	J_{sat}	2.32	0.804	1.82	0.803
	$\sigma(J_{sat})$	10.3	0.943	10.7	0.953
	skew(J_{sat})	2.45	0.852	2.75	0.923
	kurt(J_{sat})	1.28	0.811	3.99	0.943
	V_{fl}	0.879	0.496	1.57	0.743
	$\sigma(V_{fl})$	8.42	0.953	5.52	0.934
	M_{\parallel}	2.56	0.816	3.86	0.847
$(\chi; Q)_{\text{FHRP}}$		(0.55; 3.77)		(0.67; 4.08)	
Thomson scattering (TS) for divertor entrance	n	1.19	0.842	1.55	0.854
	T_e	0.43	0.858	0.83	0.872
	$(\chi; Q)_{\text{TS}}$	(0.035; 0.85)		(0.2; 0.863)	
	$(\chi; Q)_{\text{TS}}$				
Reciprocating divertor probe array (RDPA) for divertor volume	n	2.93	0.854	5.07	0.845
	T_e	2.11	0.889	2.06	0.889
	V_{pl}	1.47	0.877	1.26	0.887
	J_{sat}	3.47	0.862	2.05	0.849
	$\sigma(J_{sat})$	3.27	0.865	8.51	0.851
	skew(J_{sat})	3.27	0.812	2.34	0.789
	kurt(J_{sat})	2.86	0.9	5.0	0.921
	V_{fl}	2.17	0.657	2.04	0.77
	$\sigma(V_{fl})$	41.6	0.928	11.0	0.886
	M_{\parallel}	6.54	0.862	11.4	0.862
$(\chi; Q)_{\text{RDPA}}$		(0.91; 4.11)		(0.87; 4.13)	
Infrared camera (IR) for low-field-side target	q_{\parallel}	5.22	0.808	5.67	0.839
	$(\chi; Q)_{\text{LFS-IR}}$	(1.0; 0.404)		(1.0; 0.42)	
Wall Langmuir probes for low-field-side	n	2.56	0.81	1.48	0.786
	T_e	2.12	0.882	1.85	0.865
	V_{pl}	2.73	0.88	1.61	0.88
	J_{sat}	3.31	0.848	2.05	0.826

$\sigma(J_{sat})$	4.6	0.85	4.25	0.865	
skew(J_{sat})	2.97	0.833	42.8	0.956	
kurt(J_{sat})	4.39	0.907	40.8	0.98	
J_{\parallel}	2.23	0.619	1.12	0.668	
$\sigma(J_{\parallel})$	4.09	0.857	3.36	0.852	
V_{fl}	0.841	0.614	1.93	0.707	
$\sigma(V_{fl})$	6.87	0.91	8.83	0.925	
$(\chi; Q)_{\text{LFS-LP}}$	(0.93; 5.24)		(0.75; 5.41)		
 Wall Langmuir probes for high-field-side target	 n T_e V_{pl} J_{sat} $\sigma(J_{sat})$ skew(J_{sat}) kurt(J_{sat}) J_{\parallel} $\sigma(J_{\parallel})$ V_{fl} $\sigma(V_{fl})$	 3.55 3.52 2.04 2.62 4.3 4.36 8.66 2.17 3.6 2.51 3.19	 0.842 0.906 0.904 0.827 0.821 0.814 0.94 0.676 0.88 0.618 0.898	 1.49 1.03 1.09 2.46 4.06 11.8 19.2 1.65 3.13 0.571 15.6	 0.809 0.88 0.882 0.808 0.881 0.888 0.973 0.745 0.882 0.719 0.913
$(\chi; Q)_{\text{HFS-LP}}$	(0.98; 5.34)		(0.67; 5.5)		
Overall	$\chi; Q$	(0.83; 19.7)	(0.72; 20.4)		

These results compare favorably to the results of other simulation codes in the TCV-X21 validation study [4] and quantify observations made in earlier sections. For example, both high- and low-field target Langmuir probe measurements are better predicted in reverse field than forward field.

A significant difference that has not been discussed in earlier sections is in the parallel flow Mach number M_{\parallel} , in both the Fast Horizontally-Reciprocating Probe (FHRP) and the Reciprocating Divertor Probe Array (RDPA) diagnostics. This is consistent with the particle source (ionization) being different in simulation and experiment: In simulation the particle source in the core leads to strong flows into the divertor, whereas in experiment the particle source is close to the targets. The codes used in the original study [4], that also did not include neutrals, observed comparable differences.

It can also be seen in table 4 that in general the mean profiles (e.g. density, J_{sat} , J_{\parallel}) are better predicted than higher moments of the fluctuations (e.g. $\sigma(J_{sat})$), in common with other codes in the study [4]. It is intriguing that the transport could be better captured than the characteristics of the turbulence that is in large part responsible for the transport.

7. Conclusions

3D turbulence simulations have been performed using *Hermes-3* [15], of the TCV-X21 reference cases [4]: Two lower single-null sheath-limited TCV L-mode scenarios with opposite toroidal magnetic field directions, designated forward (favorable ∇B) and reverse (unfavorable ∇B). Electrostatic drift-reduced fluid simulations have been performed in a field-aligned coordinate system, evolving electron density, ion and electron temperatures, electron and ion parallel momentum, and vorticity with Oberbeck-Boussinesq approximation. The equations are derived from [19, 20, 21] with modifications described in Appendix A. The simulations are flux-driven, evolving total plasma quantities without separation into profiles and fluctuations, and are driven by fixed input power and particle fluxes inferred from experiment [4], 120kW and 3×10^{21} particles per second.

The simulation results reproduce many qualitative and quantitative features of experiment, without any tuning of simulation input parameters. Agreement is particularly good in the near SOL, where the expected ion sound gyro-radius spatial scales are well resolved. The computational expense of the simulations shown here was approximately 6000 core-hours per ms, running on 64 cores, with several ms of simulation time required to relax profiles to quasi-steady state. These simulations demonstrate the ability of *Hermes-3* to robustly perform long simulations of medium-sized tokamak (MST) edge turbulence at modest computational expense. Detailed analysis of the energy balance in the simulations (section 5) points to the need for further improvements in the handling of perpendicular flow energy that is related to the vorticity equation and polarisation current. Ongoing development aims to ensure that dissipated perpendicular flow energy goes into ion heating, making use of improved polarisation current formulation [23].

Differences between simulation and experiment point to the role of neutrals in cooling the divertor targets, replacing particle flux from the core with ionisation in the divertor legs. One of the conclusions of the original TCV-X21 study [4] was that despite the choice of a sheath-limited experimental regime, plasma-neutral interactions were likely influencing the turbulence in the divertor. Simulation of the TCV-X21 cases with SOLPS-ITER [38], including kinetic neutrals, found that $\sim 65\%$ of the total ionization occurs in the SOL and divertor. Those results support findings that neutrals are important even in these sheath-limited plasma scenarios. The SOLPS-ITER simulations were performed without drifts, so cannot explain differences between forward and reversed field configurations. The experimental data [38] shows higher Balmer line radiation (Divertor spectroscopy system) and higher neutral gas pressure (barotron measurements) in forward field, indicating stronger plasma-neutral interaction. Including these interactions to improve model fidelity is the subject of ongoing work.

Acknowledgements

Prepared by LLNL under Contract DE-AC52-07NA27344. This work made use of the version 1.0 of the TCV-X21 experimental datasets [6] provided by the TCV team and publicly released under the CC-BY 4.0 license. B.D. thanks Tom Body for many helpful discussions. The results shown here were produced with *Hermes-3* version 05d4d98 linked to *BOUT++* version a776c8c. *Hermes-3* (LLNL-CODE-845139) is available on Github [16] under the GPL-3 license. LLNL-JRNL-2005230.

Government Use License Notice

This manuscript has been authored by Lawrence Livermore National Security, LLC under Contract No. DE-AC52-07NA27344 with the US. Department of Energy. The United States Government retains, and the publisher, by accepting the article for publication, acknowledges that the United States Government retains a non-exclusive, paid-up, irrevocable, world-wide license to publish or reproduce the published form of this manuscript, or allow others to do so, for United States Government purposes.

References

- [1] R.A. Pitts, X. Bonnin, F. Escourbiac, H. Frerichs, J.P. Gunn, T. Hirai, A.S. Kukushkin, E. Kaveeva, M.A. Miller, D. Moulton, V. Rozhansky, I. Senichenkov, E. Sytova, O. Schmitz, P.C. Stangeby, G. De Temmerman, I. Veselova, and S. Wiesen. Physics basis for the first iter tungsten divertor. *Nuclear Materials and Energy*, 20:100696, 2019.
- [2] Frédéric Schwander, Eric Serre, Hugo Bufferand, Guido Ciraolo, and Philippe Ghendrih. Global fluid simulations of edge plasma turbulence in tokamaks: a review. *Computers & Fluids*, 270:106141, 2024.
- [3] P C Stangeby. *The Plasma Boundary of Magnetic Fusion Devices*. Plasma Physics Series. Institute of Physics Publishing, 2000.
- [4] D.S. Oliveira, T. Body, D. Galassi, C. Theiler, E. Laribi, P. Tamain, A. Stegmeir, M. Giacomin, W. Zholobenko, P. Ricci, H. Bufferand, J.A. Boedo, G. Ciraolo, C. Colandrea, D. Coster, H. de Oliveira, G. Fourestey, S. Gorno, F. Imbeaux, F. Jenko, V. Naulin, N. Offeddu, H. Reimerdes, E. Serre, C.K. Tsui, N. Varini, N. Vianello, M. Wiesenberger, C. Wüthrich, and the TCV Team. Validation of edge turbulence codes against the TCV-X21 diverted L-mode reference case. *Nucl. Fusion*, 62(9):096001, jul 2022.
- [5] B P Duval et al. Experimental research on the TCV tokamak. *Nucl. Fusion*, 64:112023, 2024.
- [6] D.S. Oliveira, T. Body, D. Galassi, C. Theiler, E. Laribi, P. Tamain, A. Stegmeir, M. Giacomin, W. Zholobenko, P. Ricci, H. Bufferand, J.A. Boedo, G. Ciraolo, C. Colandrea, D. Coster, H. de Oliveira, G. Fourestey, S. Gorno, F. Imbeaux, F. Jenko, V. Naulin, N. Offeddu, H. Reimerdes, E. Serre, C.K. Tsui, N. Varini, N. Vianello, M. Wiesenberger, C. Wüthrich, and the TCV Team. TCV-X21 validation for divertor turbulence simulations. <https://github.com/SPCData/TCV-X21>, 2022.
- [7] P Ricci, F D Halpern, S Jolliet, J Loizu, A Mosetto, A Fasoli, I Furno, and C Theiler. *Plasma Phys. Control. Fusion*, 54:124047, 2012.
- [8] F. D. Halpern, P. Ricci, S. Jolliet, J. Loizu, J. Morales, A. Mosetto, F. Musil, F. Riva, T. M. Tran, and C. Wersal. The GBS code for tokamak scrape-off layer simulations. *Journal of Computational Physics*, 315:388–408, June 2016.

- [9] A. Stegmeir, A. Ross, T. Body, M. Francisquez, W. Zholobenko, D. Coster, O. Maj, P. Manz, F. Jenko, B. N. Rogers, and K. S. Kang. Global turbulence simulations of the tokamak edge region with grillix. *Physics of Plasmas*, 26(5):052517, 2019.
- [10] W Zholobenko, T Body, P Manz, A Stegmeir, B Zhu, M Griener, G D Conway, D Coster, F Jenko, and the ASDEX Upgrade Team. Electric field and turbulence in global Braginskii simulations across the ASDEX Upgrade edge and scrape-off layer. *Plasma Physics and Controlled Fusion*, 63(3):034001, feb 2021.
- [11] P Tamain, H Bufferand, G Ciraolo, C Colin, D Galassi, Ph. Ghendrih, F Schwander, and E Serre. *J. Comput. Phys.*, 321:606–623, 2016.
- [12] F. Nespoli, P. Tamain, N. Fedorczak, G. Ciraolo, D. Galassi, R. Tatali, E. Serre, Y. Marandet, H. Bufferand, and Ph. Ghendrih. 3d structure and dynamics of filaments in turbulence simulations of west diverted plasmas. *Nucl. Fusion*, 59(9):096006, jul 2019.
- [13] H. Bufferand, G. Ciraolo, R. Düll, G. Falchetto, N. Fedorczak, Y. Marandet, V. Quadri, M. Raghunathan, N. Rivals, F. Schwander, E. Serre, S. Sureshkumar, P. Tamain, and N. Varadarajan. Global 3d full-scale turbulence simulations of tcv-x21 experiments with soledge3x. *Nuclear Materials and Energy*, 41:101824, 2024.
- [14] Philipp Ulbl, Thomas Body, Wladimir Zholobenko, Andreas Stegmeir, Jan Pfennig, and Frank Jenko. Influence of collisions on the validation of global gyrokinetic simulations in the edge and scrape-off layer of TCV. *Physics of Plasmas*, 30(5):052507, 05 2023.
- [15] B Dudson, M Kryjak, H Muhammed, P Hill, and J T Omotani. Hermes-3: Multi-component plasma simulations with BOUT++. *Comp. Phys. Comm.*, 2023.
- [16] Ben Dudson et al. Hermes-3. <https://github.com/bendudson/hermes-3>.
- [17] B D Dudson et al. BOUT++: Recent and current developments. *J. Plasma Phys.*, 81(01):365810104, 2015.
- [18] B D Dudson, W A Gracias, R Jorge, A H Nielsen, J M B Olsen, P Ricci, C Silva, P Tamain, G Ciraolo, N Fedorczak, D Galassi, J Madsen, F Militello, N Nace, J J Rasmussen, F Riva, and E Serre. Edge turbulence in ISTTOK: a multi-code fluid validation. *Plasma Phys. Control. Fusion*, 63(5):055013, apr 2021.
- [19] A N Simakov and P J Catto. Drift-ordered fluid equations for field-aligned modes in low- β collisional plasma with equilibrium pressure pedestals. *Physics of Plasmas*, 10(12):pp. 4744–4757, December 2003.
- [20] P J Catto and A N Simakov. A drift ordered short mean free path description for magnetized plasma allowing strong spatial anisotropy. *Physics of Plasmas*, 11(1):pp. 90–102, January 2004.
- [21] A N Simakov and P J Catto. Erratum: “Drift-ordered fluid equations for field-aligned modes in low- β collisional plasma with equilibrium pressure pedestals”. *Physics of Plasmas*, 11(5):p.2326, May 2004.
- [22] A B Mikhailovskii and V S Tsypin. Transport equations and gradient instabilities in a high pressure collisional plasma. *Plasma Physics*, 13(9):785, sep 1971.
- [23] Federico D. Halpern, Ronald E. Waltz, and Tess N. Bernard. Drift-ordered fluid vorticity equation with energy consistency. *Physics of Plasmas*, 30(3):032302, 03 2023.
- [24] S I Braginskii. *Transport processes in a plasma*, volume 1 of *Reviews of Plasma Physics*, page 205. 1965.
- [25] A Oberbeck. *Ann. Phys. Chem.*, 7:271, 1879.
- [26] W Zholobenko, K Zhang, A Stegmeir, J Pfennig, K Eder, C. Pitzal, P. Ulbl, M. Griener, L. Radovanovic, U. Plank, and ASDEX Upgrade Team. Tokamak H-mode edge-SOL global turbulence simulations with an electromagnetic, transcollisional drift-fluid model. *Nucl. Fusion*, 64:106066, 2024.
- [27] L. Easy, F. Militello, T. Nicholas, J. Omotani, F. Riva, N. Walkden, UKAEA. Storm drift-reduced plasma fluid model. <https://github.com/boutproject/STORM>.
- [28] Fabio Riva, Fulvio Militello, Sarah Elmore, John T Omotani, Ben Dudson, Nick R Walkden, and the MAST team. Three-dimensional plasma edge turbulence simulations of the mega

ampere spherical tokamak and comparison with experimental measurements. *Plasma Physics and Controlled Fusion*, 61(9):095013, aug 2019.

[29] P C Stangeby. The Bohm–Chodura plasma sheath criterion. *Physics of Plasmas*, 2:702, 1995.

[30] D Tskhakaya and S Kuhn. Boundary conditions for the multi-ion magnetized plasma-wall transition. *J. Nucl. Materials*, 337-339:405–409, 2005.

[31] John Omotani et al. Hypnotoad grid generator. <https://github.com/boutproject/hypnotoad>, 2019-2021.

[32] B D Dudson and J Leddy. *Plasma Phys. Control. Fusion*, 59:054010, 2017.

[33] B D Dudson, J Allen, T Body, B Chapman, C Lau, L Townley, D Moulton, J Harrison, and B Lipschultz. The role of particle, energy and momentum losses in 1d simulations of divertor detachment. 61(6):065008, may 2019.

[34] A C Hindmarsh et al. SUNDIALS: Suite of nonlinear and differential/algebraic equation solvers. *ACM Transactions on Mathematical Software*, 31(3):363–396, 2005.

[35] V Rozhansky, E Kaveeva, I Senichenkov, D Sorokina, E Vekshina, D Coster, P McCarthy, N Khromov, and ASDEX Upgrade team. Currents structure in the scrape-off layer of a tokamak. 25:100840, 2020.

[36] G M Staebler and F L Hinton. Currents in the scrape-off layer of diverted tokamaks. *Nucl. Fusion*, 29:1820, 1989.

[37] P. Ricci, F. Riva, C. Theiler, A. Fasoli, I. Furno, F. D. Halpern, and J. Loizu. Approaching the investigation of plasma turbulence through a rigorous verification and validation procedure: A practical examplea). *Physics of Plasmas*, 22(5):055704, 05 2015.

[38] Y. Wang, C. Colandrea, D.S. Oliveira, C. Theiler, H. Reimerdes, T. Body, D. Galassi, L. Martinelli, K. Lee, and the TCV Team. Validation of solps-iter simulations against the tcv-x21 reference case. *Nucl. Fusion*, 64(5):056040, apr 2024.

[39] J. Madsen, V. Naulin, A. H. Nielsen, and J. Juul Rasmussen. Collisional transport across the magnetic field in drift-fluid models. *Physics of Plasmas*, 23(3):032306, 2016.

[40] A H Nielsen, J Juul Rasmussen, J Madsen, G S Xu, V Naulin, J M B Olsen, M Løiten, S K Hansen, N Yan, L Tophøj, and B N Wan. Numerical simulations of blobs with ion dynamics. *Plasma Phys. Control. Fusion*, 59(2):025012, dec 2016.

[41] Bruce D Scott. Tokamak edge turbulence: background theory and computation. *Plasma Phys. Control. Fusion*, 49(7):S25, jun 2007.

Appendix A. Modifications to drift-reduced fluid equations

The drift-reduced fluid equations implemented in *Hermes-3* have been modified from those derived in [19, 20, 21] so that they (a) make the electrostatic approximation; (b) Have a conserved energy that includes the perpendicular ion flow, bounding the energy in plasma flows; (c) Make the Oberbeck-Boussinesq approximation, simplifying the calculation of potential ϕ from vorticity ω (equation 6).

Appendix A.1. Vorticity equation

The form of vorticity used here (equation 7) is adapted from [19, 20, 21]. Using SI units and the notation used in section 2 the vorticity equation is:

$$\frac{\partial \omega}{\partial t} = \nabla \cdot \mathbf{J}_{\parallel} + \nabla \times \frac{\mathbf{b}}{B} \cdot \nabla (p_i + p_e) \quad (1.1a)$$

$$- \nabla \cdot \left[\nabla_{\perp} \left(\frac{m_i}{2B^2} \mathbf{v}_E \cdot \nabla p_i \right) + \frac{\omega}{2} \mathbf{v}_E \right] \quad (1.1b)$$

$$- \nabla \cdot \left[\left(\frac{m_i n}{2B^2} \nabla_{\perp}^2 \phi \right) \left(\mathbf{v}_E + \frac{\mathbf{b} \times \nabla p_i}{enB} \right) \right] \quad (1.1c)$$

$$- \nabla \cdot \left[\left(\frac{m_i}{2B^2} \mathbf{v}_E \cdot \nabla n \right) \nabla_{\perp} \phi \right] \quad (1.1d)$$

$$+ \nabla \cdot \left[\frac{\mathbf{b}}{B} \times \left(\kappa \pi_{ci} - \frac{1}{3} \nabla \pi_{ci} - \mathbf{S}^M \right) \right] \quad (1.1e)$$

In the *Hermes-3* implementation the Oberbeck-Boussinesq approximation is made, so that in the polarisation current terms $n \rightarrow n_0$ (a constant), $\nabla n \rightarrow 0$, and so equation 1.1d is removed.

The other significant change is in equation 1.1b, motivated by conservation of energy. Energy transfer channels (see Appendix B) are calculated by multiplying the vorticity equation by $\left(\phi + \frac{p_i}{en_0} \right)$. The first term in equation 1.1b becomes:

$$\left(\phi + \frac{p_i}{en_0} \right) \nabla \cdot \left[\nabla_{\perp} \left(\frac{m_i}{2B^2} \mathbf{v}_E \cdot \nabla p_i \right) \right] = \nabla \cdot \left[\frac{m_i}{2B^2} \left(\phi + \frac{p_i}{en_0} \right) \nabla_{\perp} (\mathbf{v}_E \cdot \nabla p_i) \right] \quad (1.2a)$$

$$- \nabla_{\perp} \left[\frac{m_i}{2B^2} (\mathbf{v}_E \cdot \nabla p_i) \nabla \left(\phi + \frac{p_i}{en_0} \right) \right] \quad (1.2b)$$

$$+ (\mathbf{v}_E \cdot \nabla p_i) \frac{\omega}{2} \quad (1.2c)$$

$$+ \left(\phi + \frac{p_i}{en_0} \right) \nabla \cdot \left[(\mathbf{v}_E \cdot \nabla p_i) \nabla_{\perp} \left(\frac{m_i}{2B^2} \right) \right] \quad (1.2d)$$

The terms 1.2a and 1.2b are divergences, and so integrate over the domain to leave only boundary fluxes. Term 1.2c cancels the energy transfer term coming from the second term in equation 1.1b. The final term, 1.2d, is a spurious source of energy if there are gradients in the magnetic field strength B .

The polarisation current terms, including equation 1.1*b*, are derived in [19, 21] in a straight magnetic field (i.e. constant B). Consistent with that approximation, we may move the factor of B^2 through the spatial derivative in equation 1.1*b* such that 1.2*d* is removed and energy conservation restored. This leads to the form of the vorticity equation implemented in *Hermes-3* (equation 7).

Appendix A.2. Ion energy

The term $\frac{p_i}{en_0} \nabla \cdot (\mathbf{J}_{||} + \mathbf{J}_d)$ appearing in the ion thermal energy (equation B.3) is compression due to the ion polarisation velocity and viscous terms. This can be seen from quasineutrality: $\nabla \cdot (\mathbf{J}_{||} + \mathbf{J}_d) = -\nabla \cdot (\mathbf{J}_{pol} + \mathbf{J}_{ci})$. Taking the Oberbeck-Boussinesq approximation $\mathbf{J}_{pol} = en_0 \mathbf{v}_{pol}$, and so $\frac{p_i}{en_0} \nabla \cdot (\mathbf{J}_{||} + \mathbf{J}_d) \simeq -p_i \nabla \cdot \mathbf{v}_{pol}$. This term therefore adds to similar compression terms for the $E \times B$ and parallel flow.

This ion pressure term can be derived from the vorticity equation using energy conservation considerations (Appendix B), or from first principles [39] as implemented in e.g. HESEL [40]. It does not appear in the equations of Simakov & Catto [19, 20, 21] because those equations do not include the perpendicular flow in the conserved energy of the system, and polarisation drift is formally smaller than $E \times B$ drift in the drift ordering.

Appendix B. Energy conservation

The set of equations given in section 2 has a conserved energy

$$E = \int \frac{1}{2} n_0 m_i \left| \frac{\nabla_{\perp} \phi}{B} + \frac{\nabla_{\perp} p_i}{en_0 B} \right|^2 + \frac{3}{2} (p_e + p_i) + \frac{1}{2} m_i n v_{||i}^2 + \frac{1}{2} m_e n v_{||e}^2 dV \quad (B.1)$$

where the integral is over the domain volume V . This energy includes both the perpendicular and parallel flow kinetic energy.

Using the methodology of B.Scott [41], energy conservation can be evaluated by multiplying the vorticity equation by $(\phi + \frac{p_i}{en_0})$, the ion momentum equation by $v_{||i}$ and the electron momentum equation by $v_{||e}$ and rearranging. Terms that can be written as divergences of an energy flux become boundary fluxes when integrated over the domain, and so are omitted for clarity. The rate of change of the components of the energy density (left side of equations B.2 - B.6) are given by transfer channels from other components (right side):

$$\begin{aligned} \frac{\partial}{\partial t} \left[\frac{1}{2} n_0 m_i \left| \frac{\nabla_{\perp} \phi}{B} + \frac{\nabla_{\perp} p_i}{n_0 B} \right|^2 \right] &= -\phi \nabla_{||} j_{||} - \phi \nabla \cdot \left[(p_e + p_i) \nabla \times \frac{\mathbf{b}}{B} \right] \\ &\quad - \frac{p_i}{en_0} \nabla \cdot (\mathbf{J}_{||} + \mathbf{J}_d) \end{aligned} \quad (B.2)$$

$$\begin{aligned} \frac{\partial}{\partial t} \left(\frac{3}{2} p_i \right) &= -p_i \nabla \cdot (\mathbf{v}_E + \mathbf{b} v_{||i}) - W_{ei} \\ &\quad + \frac{p_i}{en_0} \nabla \cdot (\mathbf{J}_{||} + \mathbf{J}_d) \end{aligned} \quad (B.3)$$

$$\begin{aligned} \frac{\partial}{\partial t} \left(\frac{3}{2} p_e \right) &= -p_e \nabla \cdot (\mathbf{v}_E + \mathbf{b} v_{\parallel e}) + W_{ei} \\ &\quad + (v_{\parallel i} - v_{\parallel e}) F_{ei} \end{aligned} \quad (\text{B.4})$$

$$\frac{\partial}{\partial t} \left(\frac{1}{2} m_i n v_{\parallel i}^2 \right) = -v_{\parallel i} \mathbf{b} \cdot \nabla p_i + Z_i env_{\parallel i} E_{\parallel} - v_{\parallel i} F_{ei} \quad (\text{B.5})$$

$$\frac{\partial}{\partial t} \left(\frac{1}{2} m_e n v_{\parallel e}^2 \right) = -v_{\parallel e} \mathbf{b} \cdot \nabla p_e - env_{\parallel e} E_{\parallel} + v_{\parallel e} F_{ei} \quad (\text{B.6})$$

Each energy transfer channel appears either in two equations with opposite signs, or combines with other terms to form a full divergence. For example the Alfvén wave involves terms in equations B.2, B.5 and B.6. The electrostatic approximation is used in this model, so $E_{\parallel} = -\partial_{\parallel} \phi$.

$$-\phi \nabla_{\parallel} j_{\parallel} + Z_i env_{\parallel i} E_{\parallel} - env_{\parallel e} E_{\parallel} = -\phi \nabla_{\parallel} j_{\parallel} - j_{\parallel} \partial_{\parallel} \phi \quad (\text{B.7})$$

$$= \nabla_{\parallel} (\phi j_{\parallel}) \quad (\text{B.8})$$

so that when integrated over the domain these terms sum to leave only boundary fluxes. A similar identity holds for the diamagnetic drift terms responsible for energy exchange between the $E \times B$ flow energy, equation B.2, and internal energy equations B.3 and B.4:

$$-\phi \nabla \cdot \left[p_e \nabla \times \frac{\mathbf{b}}{B} \right] - p_e \nabla \cdot \mathbf{v}_E = -\phi \nabla \cdot \left[p_e \nabla \times \frac{\mathbf{b}}{B} \right] - p_e \nabla \times \frac{\mathbf{b}}{B} \cdot \nabla \phi \quad (\text{B.9})$$

$$= -\nabla \cdot \left[\phi p_e \nabla \times \frac{\mathbf{b}}{B} \right] \quad (\text{B.10})$$

This again has the form of a divergence, and so integrates over the domain to leave only boundary fluxes. The corresponding terms in the vorticity and pressure equations are implemented using central differences, so that the discrete operators for divergence and gradients obey the above analytic identity.

The term $\frac{p_i}{env_0} \nabla \cdot (\mathbf{J}_{\parallel} + \mathbf{J}_d)$ appearing in perpendicular kinetic energy (equation B.2) and ion thermal energy (equation B.3) is discussed in section Appendix A.2 above.